A Complete Spectral Polarimeter Design for Lightwave Communication Systems

Shawn X. Wang, *Student Member, IEEE*, and Andrew M. Weiner, *Fellow, IEEE*, *Fellow, OSA*

***Abstract*—The authors describe a fast spectral polarimeter operating in the lightwave communications band capable of measuring both state-of-polarization and degree-of-polarization of hundreds (up to thousands) of spectral components in parallel within milliseconds. In this paper, the design incorporates fast switching ferroelectric liquid crystals for polarization component selection on the 100-μs scale. Dispersion elements and an arrayed detector are used for wavelength-parallel sensing. Bandwidth of coverage can be scaled from a single wavelength-division multiplexed channel to more than 100 nm, and 256 spectral polarization measurements in under 1 ms are verified. Finally, a calibration algorithm is used to minimize measurement error. This instrument offers unprecedented sensing capability relevant to the monitoring and compensation of polarization-related impairments in high-speed lightwave communications.**

***Index Terms*—Degree-of-polarization (DOP), polarimetry, polarization-mode dispersion (PMD).**

I. Introduction

SPECTRAL polarimetry, or the measurement of wavelength-dependent polarization, has many interesting applications in the fields of science, medicine, and engineering. Within the last couple of decades, the explosive growth in the communications industry triggered new utilizations of spectral polarimetry for various types of system performance monitoring, e.g., polarization-mode dispersion (PMD) monitoring and compensation [1]–[4]. Current commercial polarization sensing products are mostly single channeled. It is possible to perform multiwavelength polarization measurements by using a single-channel polarization analyzer and a tunable optical filter or tunable laser, but the resulting data acquisition rate is severely constrained by the tuning and settling speed of the filter. Several lab-fabricated spectral polarimeters have been reported recently [5]–[11] due to the increase in interest for such a device. These spectral polarimeters were all reported with various design objectives: Some claimed high spectral resolution, some claimed broad bandwidth, and others claim small form factor. However, the reported spectral polarimeters all lack in speed—from seconds to minutes for a set of spectral SOP measurement. Fast spectral state-of-polarization (SOP) and degree-of-polarization (DOP) sensing are essential in certain high-bandwidth optical communication applications such as near-real-time adaptive PMD compensation applications [2], [12]. Since polarizations within a fiber have been reported to occasionally vary on a millisecond timescale or less [13], [14], fast monitoring techniques are needed. In this paper, we describe a spectral polarimeter design capable of monitoring the complete SOP and DOP for hundreds of optical wavelength components in parallel within 1 ms with no moving parts. A variation of this design has demonstrated simultaneous SOP measurements of more than 1000 spectral component at 2.8-GHz resolution with more than 20-dB isolation between spectral spacing, covering the entire lightwave communications C-band.

In Section II, we discuss the details of our initial spectral polarimeter design [15] and calibration procedure, which allowed accurate spectral measurement of normalized SOP. From here on out, we refer to SOP or normalized SOP as the normalized Stokes' vector with unit magnitude, and DOP refers to the magnitude of the Stokes' vector. Both simulated and experimental results are shown to demonstrate the performance of this device. However, this design was less suitable for performing accurate DOP measurements. In Section III, we demonstrate a reconfigured complete spectral polarimeter that allows both accurate SOP and DOP measurements. We also discuss the use of the original normalized SOP polarimeter necessary for calibration of the new polarimeter configuration. In Section IV, we briefly describe a high-resolution version of the polarimeter that is capable of resolving spectral SOP variation within each dense wavelength-division multiplexed (DWDM) channel. Finally, we summarize in Section V.

II. Normalized Spectral SOP Measurement

In a typical polarimeter, the intensity of four polarization components of interest of the light under test (LUT) are measured—linearly polarized 0° (I_0), 90° (I_{90}), 45° (I_{45}), and the right-hand circular polarization (I_{RHC}). The Stokes' parameters (S_0, S_1, S_2, and S_3) describing the complete SOP of the incident light can be determined from the four polarization component measurements by the following equations [16]:

$$S_0 = I_0 + I_{90} = I_{45} + I_{135} = I_{\mathrm{RHC}} + I_{\mathrm{LHC}} \tag{1}$$

$$S_1 = I_0 - I_{90} \tag{2}$$

$$S_2 = I_{45} - I_{135} = 2I_{45} - S_0 \tag{3}$$

$$S_3 = I_{\mathrm{RHC}} - I_{\mathrm{LHC}} = 2I_{\mathrm{RHC}} - S_0. \tag{4}$$

There are two basic types of polarimeter designs: 1) the division of amplitude and 2) the time sequential measurements.

Manuscript received April 7, 2006; revised July 14, 2006. This work was supported by the National Science Foundation under Grant 0501366-ECS.

The authors are with the School of Electrical and Computer Engineering, Purdue University, West Lafayette, IN 47907 USA (e-mail: wang7@ecn.purdue.edu; amw@ecn.purdue.edu).

Color versions of Figs. 2–17 are available online at http://ieeexplore.ieee.org.
Digital Object Identifier 10.1109/JLT.2006.883614

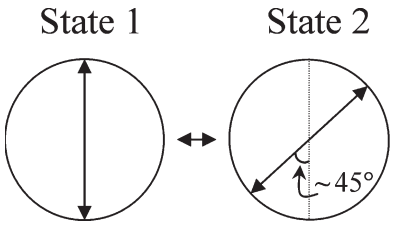

Fig. 1. FLC switching pattern.

TABLE I
SWITCHING SEQUENCE OF THE TWO-FLC POLARIMETER

Switching sequence of the two-FLC polarimeter				
input SOP	1st FLC fast axis	intermediate SOP	2nd FLC fast axis	output SOP
0°	90°	0°	0°	0°
90°	135°	RHC	135°	0°
45°	90°	RHC	135°	0°
RHC	135°	0°	0°	0°

Our design belongs to the latter, in which the input polarization is typically altered using a set of adjustable waveplate(s) and analyzed using a polarizer. By cycling through a predetermined sequence of input polarization alterations, a detector can then sequentially measure the intensities of different polarization components of interest at the output of the polarizer. Our design employs two major advancements over typical polarimeters—the use of fast switching ferroelectric liquid crystal (FLC) retarders and a spectral disperser with an arrayed detector. Also, because no mechanical movements are required to make a measurement, the system is capable of precise and repeatable measurements for each wavelength channel.

A switchable FLC retarder has two stable optic-axis orientations, separated by approximately 45° as shown in Fig. 1, [17], [18]. Its optic axes can be switched from one orientation to the other with a typical 0%–90% transition time of 70 μs [18]. Two such switchable retarders can be used to produce four different switching states. Magneto-optic crystals have also been shown to be used for polarization switching with an even faster response [19], but for this report, we chose to work with FLCs due to their availability and ease of use. After numerical simulation on various FLC specifications and switching combinations, it was found through numerical simulations that two quarter-wave FLC retarders could be used to yield a desired set of polarization alterations. The first FLC is aligned so that the fast axis switches between 90° and 135° and the second FLC switches between 135° (equivalent to $-45°$) and 0°. As shown in Table I, 0°, 90°, 45°, and RHC polarization components can be sequentially altered to become 0°. A 0° polarizer can then be placed subsequently to the FLCs to filter out the intensities of these polarization components of interest to be measured.

In the experimental setup shown in Fig. 2, two zero-order quarter-wave FLC cells (Displaytech LV1300-OEM) were used to manipulate the polarization of the incident light, causing different polarization components to sequentially pass the linear polarizer. The polarizer was oriented along 0° because the lowest polarization-dependent loss (PDL) for the grating was in the TM direction (horizontal in our setup). After passing the polarizer, the light was spectrally dispersed using a

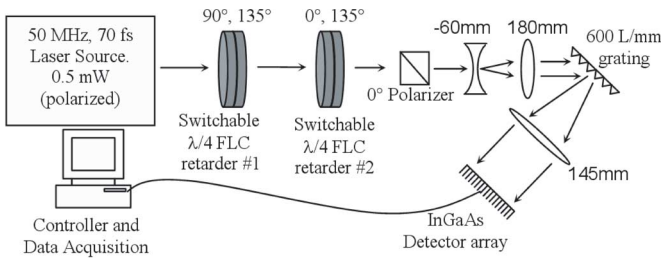

Fig. 2. Experimental setup of the wavelength-parallel polarimeter.

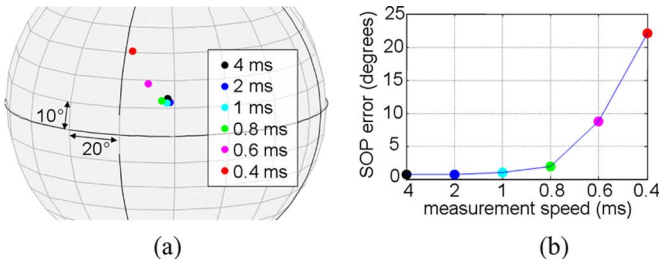

Fig. 3. (a) SOP measurements taken at different measurement speeds shown on Poincarè sphere. (b) SOP measurement errors at different speeds.

600-line/mm grating and 145-mm focal length lens onto a 256-pixel linear InGaAs detector array (Sensor's Unlimited, SU256LX-17T1-0500-A/H). The grating was aligned at an incident angle of $\sim$13° with $\sim$5° of dispersion angle between 1520- and 1630-nm light, and the arrayed detector had 50-μm pixel pitch and 500-μm pixel height. The spot size on the grating was $\sim$12 mm in diameter. Our setup resulted in a 110-nm wavelength span from 1520 to 1630 nm falling on the detector array with 0.4 nm of resolution at better than $-$20-dB crosstalk between pixels. We chose a large wavelength span to study wavelength dependence of our polarimeter, but a different wavelength range and spectral resolution can be selected by altering the spectral dispersion setup: Diffraction gratings can yield full-width at half-maximum (FWHM) resolution of 1.25 GHz (0.01 nm) as in a typical high-resolution optical spectrum analyzer, and a virtually imaged phased array (VIPA) with FWHM spectral resolution of $\sim$600 MHz (4.8 pm) has been reported [20]. We used our detector array with a 52-μs readout time and with a typical total input power of 0.5 mW ($\sim$2 μW per pixel). By using a waveform generator as a triggering source, we were able to demonstrate the $<$ 1-ms measurement speed of the polarimeter. Fig. 3(a) shows measured SOP data of an arbitrary polarization taken at different measurement speeds. Four different SOP component measurements complete one full set of SOP measurement, where the full set was taken within the specified timescale. Each color-coded dot represents an average of 256 spectral SOP measurements within 110-nm wavelength span all with the same SOP. As can be shown in Fig. 3(a) and (b), the results were consistent until the speed of the full measurement cycle was pushed to below 0.8 ms (0.2 ms per polarization component). We attribute the corrupted SOP observed for 0.6- and 0.4-ms measurement cycles to insufficient settling of the FLCs prior to readout via the array detector.

Tests were performed to examine the spectral SOP measurements of the polarimeter. First, polarization-maintaining

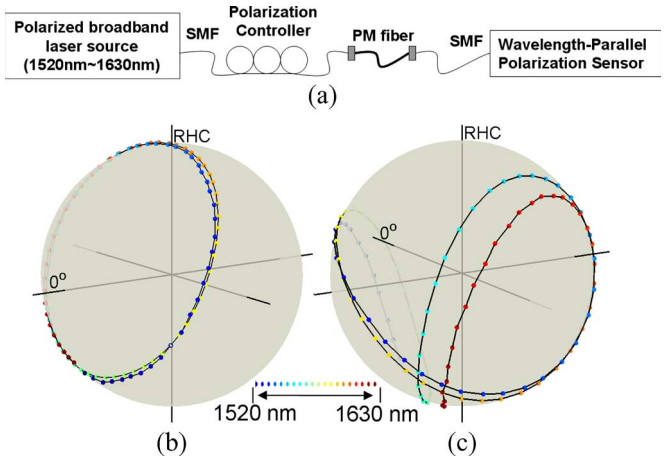

Fig. 4. (a) Single piece of 10-cm PM fiber used for producing wavelength-dependent SOP. (b) Measured output SOP of a 10-cm PM fiber. (c) Measured output SOP of two concatenated pieces of PM fibers.

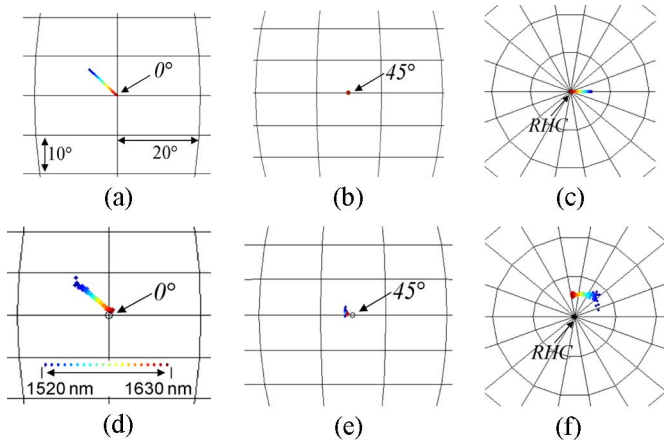

Fig. 5. Comparison of (a)–(c) simulated measurement results to (d)–(f) experimentally measured results for three of the six known test polarizations: 0°, 45°, and RHC. The results shown here are plotted on different zoomed-in sections of Poincarè spheres. 90°, 135°, and LHC exhibited similar patterns to 0°, 45°, and RHC, respectively, and are not shown.

(PM) fibers were used as wavelength-dependent polarization distorting element [Fig. 4(a)]. The PM fiber used had ∼3.5-mm beat length at 1550 nm, which is the length over which an input polarization rotates through 360°, also given by the equation $L_B = \lambda/\Delta n$, where Δn ($\Delta n \approx 4.43 \times 10^{-4}$) is the difference in refractive index between the fast and slow axes or principle states of polarization (PSP) of the birefringent fiber at wavelength λ. When a polarized broadband laser source is launched into this piece of PM fiber, it is expected that the output polarization will spread out in wavelength and rotate around the Poincarè sphere in a circular fashion, centered at the PSP of the PM. When 10 cm of such PM fiber (DGD ≈ 0.15 ps) was used, it provided roughly two full waves of phase retardation difference between 1520- and 1630-nm wavelengths, causing the output spectral SOP to loop twice around the Poincarè sphere. When the input polarization state was changed via a polarization controller at the input of the PM fiber, the circle became larger or smaller on the surface of the Poincarè sphere but always centered at the PSP. At one particular input polarization, the resultant SOP was captured and shown in Fig. 4(b), which agreed with expectation. To examine the validity of the polarimeter for any polarization around the Poincarè sphere, we performed another measurement on spectral SOP data resulting from two concatenated PM fibers with slightly different lengths and misaligned optic axes. The PSP of this new polarization distorter is now wavelength dependent, and hence, the output SOP shown in Fig. 4(c) exhibits a more complicated trajectory on the sphere as a function of wavelength, which is as qualitatively expected.

A simple method for evaluating the SOP measurement accuracy of a polarimeter is to compare the measurement results to those of a commercially available polarimeter. However, the accuracy assessed is relative to the accuracy of the reference polarimeter. Since commercially available polarimeters are single channeled, it is cumbersome to test each wavelength independently using a tunable laser source or a filter. Therefore, we performed accuracy assessment by measuring user-defined input polarization states—0°, 45°, 90°, 135°, RHC, and LHC. These SOP points were evenly distributed on the Poincarè sphere. The linear polarizations were generated by rotating a Polarcor polarizer (< 50-dB extinction ratio) to each of the four different linear polarization angles. The circular polarizations were generated by using an achromatic quarter-wave plate (QWP; OFR RMA-1/4-IR) succeeding the linear polarizer. Both the polarizer and QWP were mounted on rotation mounts with 10 arcmin resolution. The circularity of the produced light was not perfect due to slight wavelength dependence of the QWP; a quarter-wave Fresnel rhombus may be used instead of a QWP for best achromatic results.

Fig. 5 shows both numerically simulated measurement results [Fig. 5(a)–(c)] and experimental measurement results [Fig. 5(d)–(f)] of measuring three out of the six known test polarizations. The SOP measurement simulations were done in Matlab. The FLCs were simulated as Mueller matrices of birefringent phase retarders with optic axes switching by exactly 45°. The simulated retarders have quarter-wave retardance at 1630 nm to closely match the center wavelength of the actual FLCs used. The wavelength-dependent effects of the FLCs were taken into consideration, which resulted in the wavelength spread as shown in Fig. 5(a) and (c) for the 0° and RHC polarizations. Fig. 5(b) shows that 45° (same for 135°) polarization measurement happens to be wavelength insensitive for this particular FLC arrangement. Experimentally, we can see in Fig. 5(e) that all 256 points representing 256 different spectral SOP samples clustered around a single spot at the 45° point on the Poincarè sphere as expected. It is shown in these figures that simulations predicted the actual measurement results very well for the linear polarizations. There were roughly 5° of differences on the Poincarè sphere between simulated and actual measurement results for the circularly polarized lights due to imperfectly produced circular polarization mentioned earlier and also from nonideal FLC switching angles, which will be discussed later. The worst case measurements were observed for 0° and 90° measured lights—more than 10° of deviation on the Poincarè sphere at extended wavelengths from the actual SOP. Measurements around 1630 nm show close to perfect results because of the near-exact quarter-wave retardance of the

FLCs at that wavelength. Ideally, each step in our measurement sequence is designed to independently yield values for I_0, I_{90}, I_{45}, and I_{RHC}, respectively. However, due to nonideal behaviors of the FLC cells, errors were introduced into the measurements as can be shown in Fig. 5. First, the birefringences of the FLC cells were fixed; therefore, their phase retardations varied with wavelength, resulting in a wavelength-dependent system. Second, the FLC cells switched close to but not exactly by 45° due to the physics of the liquid crystals [21]. However, these errors can be minimized by applying a software correction algorithm to the measured data. Since the corrections were done on a wavelength-by-wavelength basis using the same procedure, only single-wavelength treatment will be discussed here for simplicity.

In the first step of the calibration process, measurements for six different reference polarization states are taken in a procedure discussed previously for testing measurement accuracy, i.e., 0°, 45°, 90°, 135°, RHC, and LHC. More SOP points may be used for improved calibration accuracy, but at a cost of processing time. Those six SOP points are chosen because they are easy to produce and symmetrically cover the entire Poincarè sphere.

From each of the measurements at polarization state p, four intensity values are obtained from the polarimeter, giving the intensity vector $[I^p] = [I_0^p \ I_{90}^p \ I_{45}^p \ I_{\mathrm{RHC}}^p]^T$ corresponding to the four states of the FLC pair in Table I. Using the fact that the input polarization is known, the Stokes' vector $[S^p]$ of the input can be constructed, e.g., for 0° input polarization, $[S^0] = [1\ 1\ 0\ 0]^T$. By introducing a polarimeter transformation matrix $[M]$ that we wish to calibrate, we can construct the following equation [16]:

$$[I^p] = [M][S^p]. \tag{5}$$

The values of $[I^p]$ are measured, whereas the values of $[S^p]$ are known. Since $[M]$ is 4×4, and each known input polarization state results in four measurement values (four elements of $[I]$, four different input polarizations are needed to completely determine $[M]$. We use six input polarizations, which overconstrain $[M]$. Therefore, we use the estimate for $[M]$ with minimum least squared error, given by

$$[M] = [I^{\mathrm{ref}}][S^{\mathrm{ref}}]^{\dagger} \tag{6}$$

where $[I^{\mathrm{ref}}] = [[I^0] \ \cdots \ [I^{\mathrm{LHC}}]]$ is the intensity matrix containing measurements from all six reference polarization states, $[S^{\mathrm{ref}}] = [[S^0] \ \cdots \ [S^{\mathrm{LHC}}]]$ contains the corresponding Stokes' vectors, and $[S^{\mathrm{ref}}]^{\dagger} = [S^{\mathrm{ref}}]^T([S^{\mathrm{ref}}][S^{\mathrm{ref}}]^T)^{-1}$ is the pseudo-inverse of $[S^{\mathrm{ref}}]$ [22].

Once $[M]$ is obtained, we can calibrate any measured unknown input polarization directly from the measured intensity vector using the inverse of (5), i.e.,

$$[S_{\mathrm{in}}] = [M]^{-1}[I_{\mathrm{out}}] \tag{7}$$

where $[I_{\mathrm{out}}]$ is the set of four detector readings corresponding to the four states of the FLC pair. For a single wavelength, $[M]^{-1}$ is a two-dimensional (2-D) matrix. When performing wavelength-parallel calibration for all wavelengths simultaneously, an extra dimension should be applied to the matrix calculations to account for the multiple wavelengths.

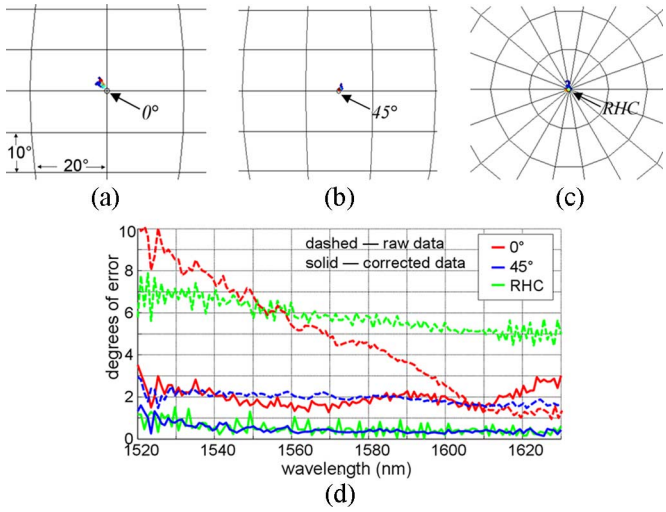

Fig. 6. Corrected measurements of (a) 0°, (b) 45°, and (c) RHC spectral SOP plotted on zoomed-in Poincarè spheres. (d) Respective errors compared to the error of the raw data. 90°, 135°, and LHC exhibited the same error figures as 0°, 45°, and RHC, respectively, and are not shown here.

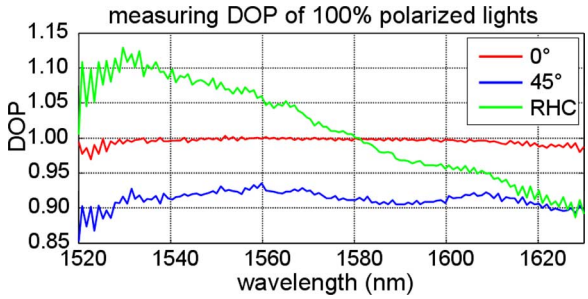

Fig. 7. Wavelength and polarization dependences of DOP measurements.

Since we are working with ∼100% polarized light (DOP ≈ 1), all SOP points show up on the surface of the unit-radius Poincarè sphere, and we express the measurement error as the angle between the actual and the measured Stokes' vectors in degrees [23].

Fig. 6(a)–(c) shows some samples of the corrected spectral SOP on the Poincarè sphere, and the amount of SOP error is shown respectively in Fig. 6(d). As the error figures show, after the calibration procedures were performed on the measured (raw) data, the corrected data of the six measurements were much improved. The raw measurement data exhibited more than 10° of error in some cases. After the calibration, 0° and 90° polarization states showed the worst measurement accuracy with an error of roughly 2° on the Poincarè sphere within the tested wavelength range. Polarization states away from 0° and 90° resulted in much more accurate measurements, and wavelength dependence was virtually eliminated. The $< 2°$ of uncorrected error were most likely due to system noise, electrical crosstalk between neighboring detector pixels, and detector nonlinearity, which could not be removed easily (Fig. 7).

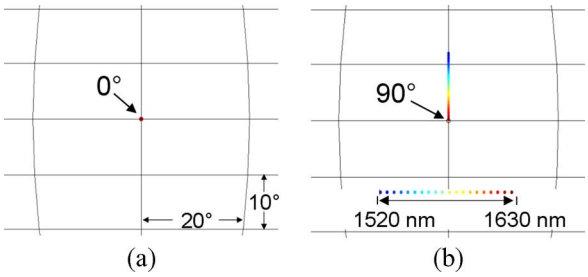

Fig. 8. (a) Measured 0° polarization component. (b) Measured 90° polarization component.

III. Complete Spectral Polarimeter Design

The SOP correction procedure worked well under the assumption that the LUT was near 100% polarized, in which case s_1, s_2, and s_3 were normalized by dividing by s_0, where $s_0 = (s_1^2 + s_2^2 + s_3^2)^{1/2}$. However, the DOP measurements were not corrected. To measure actual DOP, we could no longer assume 100% polarized light. Fig. 7 shows the actual DOP measurements of 0°, 45°, and RHC polarized lights using the DOP equation $DOP = \sqrt{s_1^2 + s_2^2 + s_3^2}/s_0$, where $s_0 = I_{\text{total}} = I_0 + I_{90}$ (using the measurement values of I_0 and I_{90}). Since the LUT was polarized, DOP should be 100%, but for polarization states such as 45° and RHC, the DOP measurements exhibit up to ±10% of error within the 110-nm wavelength range. These errors were again caused by the imperfect FLC switching angles and the wavelength dependence of the device. The measurement results did not sufficiently well preserve the orthogonality of 0° and 90° input polarization components at each wavelength, resulting in wavelength- and SOP-dependent errors in determination of the total power I_{total} (or S_0). Since DOP is defined as power of polarized portion of the LUT divided by the total power of LUT, DOP measurements incurred both wavelength- and SOP-dependent errors as well. Summarizing, these errors in DOP arise because the sum of the measured values for I_0 and I_{90} fail to give a sufficiently accurate estimate of total power. (In principle, this problem could be overcome by performing an independent spectrally resolved measurement of total power prior to the polarizer, but this is not compatible with our goal of a fast spectral polarimeter design without moving parts and with only a single detector array.)

The failed orthogonality preservation of 0° and 90° component selections can be visualized by the simulation results in Fig. 8(a) and (b), which shows 0° and 90° polarization components selected by the FLC-polarizer set in the first and second switching states of Table I. The same simulation conditions were used as those shown in Fig. 5(a)–(c). In the first switching state, the optic axes of the FLC pair are orthogonal and have a net birefringence of 0, allowing 0° polarization component to directly pass the 0° polarizer with no wavelength dependence, thus showing as a dot in Fig. 8(a). However, measuring 90° component [Fig. 8(b)] requires the optic axes of the quarter-wave FLC pair to line up to form a half-wave retarder as indicated in the second step of Table I, thus adding up the wavelength-dependent effects of each FLC as well. It can be shown that only at designed wavelength of the FLCs $\lambda = 1630$ nm, the two components selected by the instrument are exactly orthogonal, but not at other wavelengths.

In a new complete polarimetry scheme, we adapted two new concepts to our previous SOP-only polarimeter. First, we eliminated wavelength dependence in total power measurement by finding a new switching combination of the FLC pair, which allowed the measurement to better preserve the orthogonality of a pair of orthogonal input polarization components at every wavelength. Second, we found a scheme in which our previously designed SOP-only spectral polarimeter could be used to measure the precise wavelength-dependent polarization transformations involved in the operation of the new complete polarimeter and, hence, to precisely calibrate the mapping between raw measurement data and actual SOP/DOP.

Once again, all possible combinations of FLC switching sequences were numerically simulated in search of an FLC orientation, which would select orthogonal polarization states for wavelength range near the designed wavelength of the FLC pair. We used a new set of FLCs for this experiment, which had quarter-wave retardance crossing at around 1600 nm. The spectral sensing was set up to cover the C-band at that time; thus, the simulated bandwidth was from 1525 to 1565 nm. It was found that when the FLC pairs are oriented so that their fast axes both switch between 67.5° and 112.5° [Fig. 10(a)], the setup measures polarization components near 45° and 135°, as well as two elliptical states with spectrally averaged normalized Stokes' parameters of (0.453, −0.499, 0.738) and (0.453, 0.499, −0.738), as shown in Fig. 9(b)–(e). Since orthogonal polarization states show up on opposite sides of the Poincarè sphere, the two wavelength-dependent polarization components measured can be illustrated [in Fig. 9(b) and (c)] as mirror images of each other on the opposite sides of the Poincarè sphere with respect to the origin. This mirror image behavior is in clear contrast to the data of Fig. 8. The near 45° (or 135°) component and the other two elliptical polarization components measured are all linearly independent of each other in the Stokes' space, necessary for determination of the Stokes' parameters of the LUT.

Realizing that the four new polarization components (shown in Fig. 10 as red dots) measured span the Stokes' space, it is possible to take SOP measurements using a new wavelength-dependent coordinate system $(V_{1(\lambda)}, V_{2(\lambda)}, V_{3(\lambda)})$, represented in red axes in Fig. 10, and then transform back to the Stokes' coordinates (S_1, S_2, S_3), shown in blue. We defined the new system as

$$v_{0(\lambda)} = I_{\text{total}(\lambda)} = I_{\sim 45(\lambda)} + I_{\sim 135(\lambda)} \tag{8a}$$

$$v_{1(\lambda)} = I_{\sim 45(\lambda)} - I_{\sim 135(\lambda)} \tag{8b}$$

$$v_{2(\lambda)} = 2I_{\sim \text{ellip1}(\lambda)} - v_{0(\lambda)} \tag{8c}$$

$$v_{3(\lambda)} = 2I_{\sim \text{ellip2}(\lambda)} - v_{0(\lambda)} \tag{8d}$$

$$\hat{v}_{1(\lambda)} = \frac{v_{1(\lambda)}}{v_{0(\lambda)}}, \tag{8e}$$

$$\hat{v}_{2(\lambda)} = \frac{v_{2(\lambda)}}{v_{0(\lambda)}}, \tag{8f}$$

$$\hat{v}_{3(\lambda)} = \frac{v_{3(\lambda)}}{v_{0(\lambda)}}. \tag{8g}$$

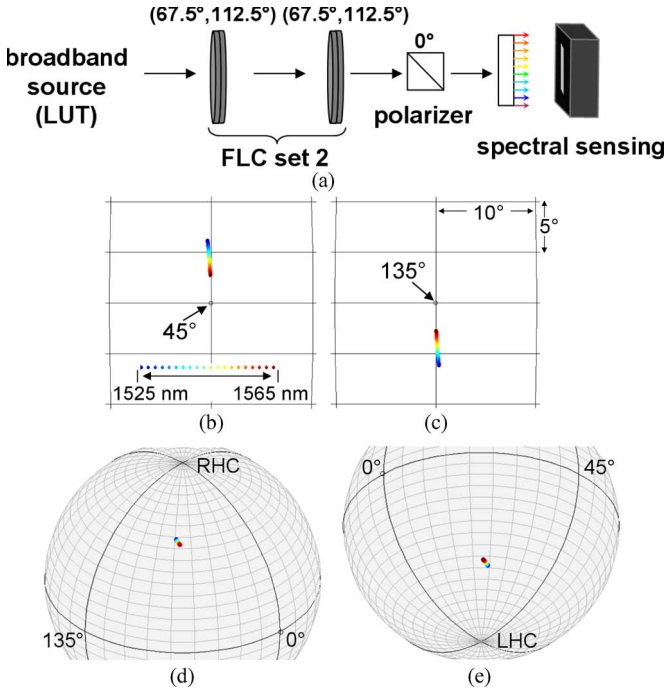

Fig. 9. (a) Wavelength-parallel polarimeter with new FLC setup. (b)–(d) Simulated results of wavelength-dependent polarization components measured with the new FLC setup, i.e., the polarization components fully passed by the polarizer after transformation by the FLC pair: (b) $\sim 45^\circ$ component. (c) $\sim 135^\circ$ component. (d) First elliptically polarized component. (e) Second elliptically polarized component.

In (8), $I_{\sim p}$ represents the intensity measurement of the polarization component near the polarization state p, and $\hat{v}_{(\lambda)} = [\hat{v}_{1(\lambda)}\ \hat{v}_{2(\lambda)}\ \hat{v}_{3(\lambda)}]^T$ is a normalized vector in the V coordinate system representing the measured polarization state of the LUT at wavelength λ.

For each wavelength, we define a linear transformation matrix $[M_{\rm vs}]_{3\times 3}$ to transform SOP of the LUT measured as $[\hat{v}]_{3\times 1}$ back to $[\hat{s}]_{3\times 1}$, i.e.,

$$[M_{\rm vs}] = \begin{bmatrix} \hat{s}_1^{v_1} & \hat{s}_2^{v_1} & \hat{s}_3^{v_1} \\ \hat{s}_1^{v_2} & \hat{s}_2^{v_2} & \hat{s}_3^{v_2} \\ \hat{s}_1^{v_3} & \hat{s}_2^{v_3} & \hat{s}_3^{v_3} \end{bmatrix}. \tag{9}$$

The first, second, and third rows of $[M_{\rm vs}]$ are the normalized Stokes' vectors for coordinate axes V_1, V_2, and V_3, respectively. Finally, we get the normalized Stokes' vector representation of the SOP, i.e.,

$$[\hat{s}] = [M_{\rm vs}]^{-1}[\hat{v}]. \tag{10}$$

Since $s_0 = I_{\rm total} = v_0$, DOP is now calculated as

$$\text{DOP} = \sqrt{\hat{s}_1^2 + \hat{s}_2^2 + \hat{s}_3^2}. \tag{11}$$

At this point, SOP is calculated from directly mapping between raw measurement data and actual SOP. However, in experiments, small amount of errors can be expected from various system aspects, such as not being able to obtain perfect V coordinates for each wavelength. Therefore, after $[\hat{s}]$ is obtained, an additional step of SOP correction can be used to further improve

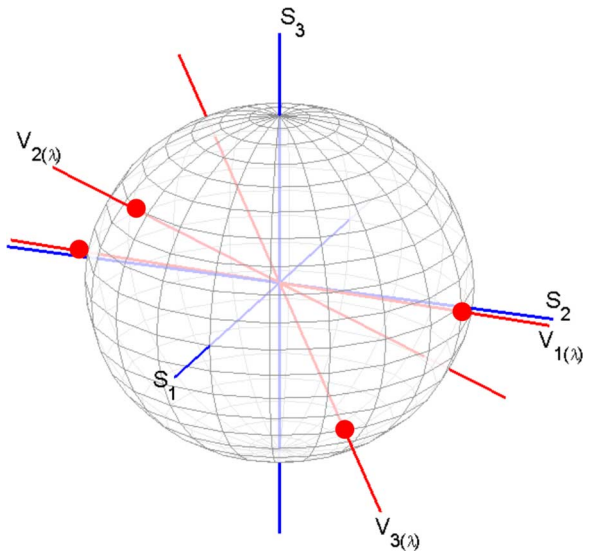

Fig. 10. $V_{(\lambda)}$ coordinate system in the Stokes' space. The red dots represent the four polarization components selected by the new FLC alignment.

the accuracy of the $[\hat{s}]$ measurement. Using a similar approach as for the earlier described SOP-only polarimeter design, we performed measurements on six known test polarization states around the Poincarè sphere. By knowing the polarization states measured, we determined a correction matrix $[M_{\rm ss}]$ for each wavelength to improve the raw SOP measurement, i.e.,

$$[\hat{s}_{\rm corrected}] = [M_{\rm ss}]^{-1}[\hat{s}]. \tag{12}$$

In our experiment, the normalized Stokes' vectors for coordinate axes $V_{1(\lambda)}$, $V_{2(\lambda)}$, and $V_{3(\lambda)}$ needed for the transformation matrix $[M_{\rm vs}]_{(\lambda)}$ were obtained by using the SOP-only polarimeter described in the last section. We ran the new FLC setup in reverse direction with a broadband amplified spontaneous emission (ASE) source as shown in Fig. 11(a), so that we could measure the polarization at the input end of the new spectral polarimeter setup [point P in Fig. 11(a)] after each of the four FLC switching combinations; this is equivalent of measuring the four what-would-be-selected polarization components by the new setup containing FLC set 2 when the new setup is run in the intended forward direction during a measurement operation. In Fig. 11(b) and (c), we see that the two nearly orthogonal polarization components selected by the new polarimeter setup are near 45° and 135° polarizations, and the measurements indeed nearly preserved their orthogonality over the full wavelength band to within 1° on the Poincarè sphere. The other two elliptical polarization components are plotted in Fig. 11(d) and (e), respectively, and their spectrally averaged normalized Stokes' parameters are (0.444, −0.470, 0.762) and (0.423, 0.495, −0.760), respectively. These measured results closely agree with the simulated results shown in Fig. 9.

The less than 1° of error was mostly due to imperfect 45° switching angle of the FLCs and resulted in a small polarization dependence of the measured $I_{\rm total}$. To verify this effect, we performed a simulation of imperfectly switched FLCs. The $I_{\rm total}$ error (ε) calculated from summing $I_{\sim 45}$ and $I_{\sim 135}$ measurements of test polarization states was shown in Fig. 12(a).

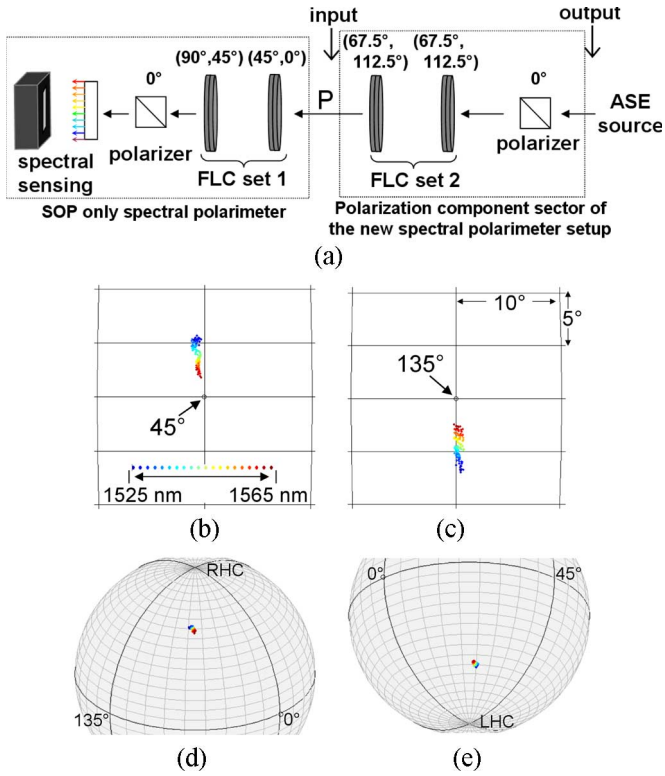

Fig. 11. (a) Measuring polarization components by running the FLC setup in reverse and measuring the reversed output with a spectral polarimeter. (b) and (c) Zoomed-in plots of the measured ∼45° and ∼135° polarization components to show the orthogonality preservation. (d, e) Two wavelength-dependent elliptical components measured.

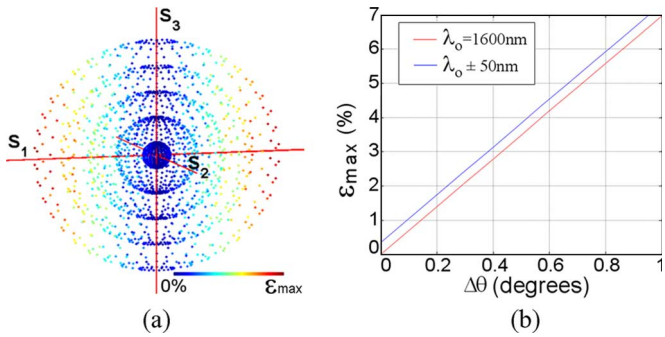

Fig. 12. (a) Polarization dependence of I_{total} measurement error. Each dot represents a polarization state; the five different spherical shells represent five different DOP settings from 20% (inner) to 100% (outer). (b) Simulated results showing maximum I_{total} error $\varepsilon_{\max}$ due to FLC switching angle defect, as well as slight wavelength dependence of $\varepsilon_{\max}$ within 100-nm range of λ_o.

The simulations were performed for 3240 different SOP points around the sphere with five different DOP settings ranging from 20% to 100%, shown in dots. The amount of error ε measurement for each SOP point is color coded from 0 to maximum I_{total} error $\varepsilon_{\max}$, and it was found that I_{total} error ε has a linear dependence only on S_1 and is essentially independent of S_2, S_3, and wavelength. Using the known ε and S_1 relationship, it is possible to correct for I_{total} measurements with the measured S_1 values. The simulated FLCs switched between $67.5 + \Delta\theta$ and $112.5 - \Delta\theta$, where $\Delta\theta$ is the small FLC defect in switching angle that is directly related to the value of $\varepsilon_{\max}$. Fig. 12(b) shows that $\varepsilon_{\max}$ has a linear relationship with $\Delta\theta$ and has a

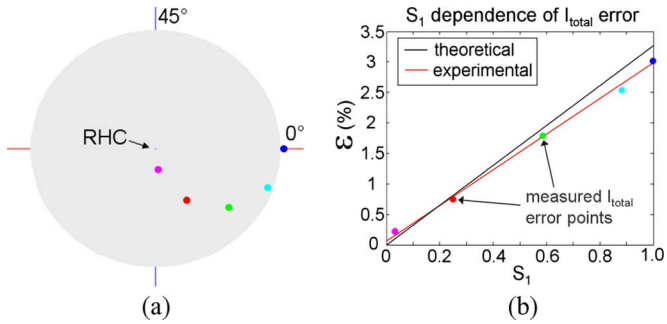

Fig. 13. (a) Theoretically produced polarizations for testing S_1 dependence of I_{total}. (b) S_1 dependence of measured ε [color coded to match SOPs in (a)].

slight wavelength dependence of up to only 0.3% within the 100-nm wavelength range near $\lambda_o \approx 1600$ nm of the FLCs.

Back to the experiment, polarization dependence of ε was checked to see if it was in fact linearly dependent only on S_1 measurement as predicted. An ASE source was passed through a 0° polarizer and a QWP to generate different test polarization states. The QWP was rotated from 0° to 50°, and SOP measurements were taken at every 10°. The theoretically produced test polarization states are plotted on the Poincarè sphere in Fig. 13(a). When the measured ε were plotted against the theoretical S_1 of the test polarization states as shown in Fig. 13(b), the results matched our prediction of a linear dependence between S_1 and ε. At $S_1 = 1$, $\varepsilon_{\max} = 3\%$, suggesting that $\Delta\theta \approx 0.4°$ based on Fig. 12(b). From an independent experimental verification of FLC switching angles, we found that the two FLCs in FLC set 2 had $\Delta\theta$ values of 0.35° and 0.5°, from which we plotted the theoretical S_1 dependence of ε. This predicts $\varepsilon_{\max} = 3.25\%$, which is again very close to the 3% from our measurement. Similar comparison tests were done with only a polarizer rotating every 10° to produce linear polarizations between 0° and 180°, and the measured ε also closely agreed with the theoretical value.

The 100% polarized polarization states were produced for a first evaluation of the performance of the new polarimeter setup. First, a Polarcor polarizer was used to produce linearly polarized light from a ∼40-nm bandwidth ASE source. The polarizer was rotated at every 10° to generate SOPs around the equator of the Poincarè sphere. In Fig. 14(a), the small circles represent the known test SOPs, and the tightly clustered colored dots near or within each of the circles are corrected spectral SOP measurements of the test SOPs; the tightness of the clusters show that they are not wavelength sensitive. Fig. 14(c) shows that the spectrally averaged linear SOP errors are all less than 1.4° for different test polarizations, which is comparable to our old polarimeter setup. To calculate DOP of 100% polarized lights, raw I_{total} were corrected using I_{total} error versus S_1 relationship shown in Fig. 13(b) to give a better estimate of v_0 (or s_0). As shown in Fig. 14(e), DOP errors were reduced to within ±3.5%. Because only a slight overall wavelength dependence of the DOP measurement was observed within the wavelength range of interest, the plot in Fig. 14(e) shows spectrally averaged DOP. However, there were up to ±0.5° of fluctuations in spectral SOP error and up to ±1% in spectral DOP measurements due to the camera readout noise. Although

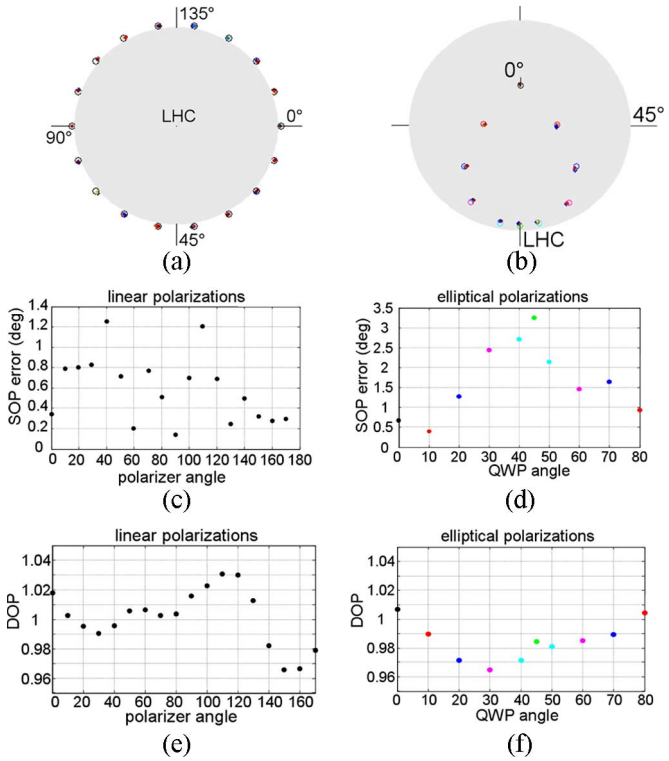

Fig. 14. (a) Measurements of generated linear polarizations around the equator of the Poincarè sphere. (b) Measurements of generated elliptical polarizations on the Poincarè sphere. (c) and (d) Spectrally averaged SOP measurement errors of polarization states shown in (a) and (b). (e) and (f) Spectrally averaged DOP measurements of 100% polarized polarization states shown in (a) and (b).

total power measurements were corrected, DOP errors were not completely eliminated due to the small amount of error contributed from S_1, S_2, and S_3 measurements.

Left-hand elliptical polarization states were also tested by placing a rotating QWP after a fixed 0° polarizer in the same manner that the I_{total} errors were tested earlier. The test polarizations produced are shown in Fig. 14(b) in a clockwise fashion starting from 0° point. As shown in Fig. 14(d), SOP errors were all less than 3.5°, and DOP errors [Fig. 14(f)] were all kept to below ±3.5% with unnoticeable overall wavelength dependence, again showing a significant improvement from the original polarimeter setup. Right-hand elliptical polarization states were also tested and showed similar measurement accuracy.

To evaluate DOP measurements of partially depolarized lights, we produced lights with known DOP and measured them using the polarimeter. To generate a depolarized light source, we first split an ASE source into two arms: with one arm polarized using a polarizer and the other arm a completely depolarized ASE source as shown in Fig. 15(a). The powers in each arm were adjusted using attenuators, and the two arms were eventually coupled back to produce partially depolarized light with DOP ranging from 0 to 1. Actual DOP was calculated from detector readings of power from each arm using the equation $\text{DOP} = P_{\text{polarized}}/(P_{\text{polarized}} + P_{\text{unpolarized}})$, where $P_{\text{polarized}}$ and $P_{\text{unpolarized}}$ are the powers of the polarized and unpolarized arms, respectively. As can be shown in Fig. 15(b), each cluster of points within the Poincarè sphere represents one set of 256 spectral polarization measurements of the partially

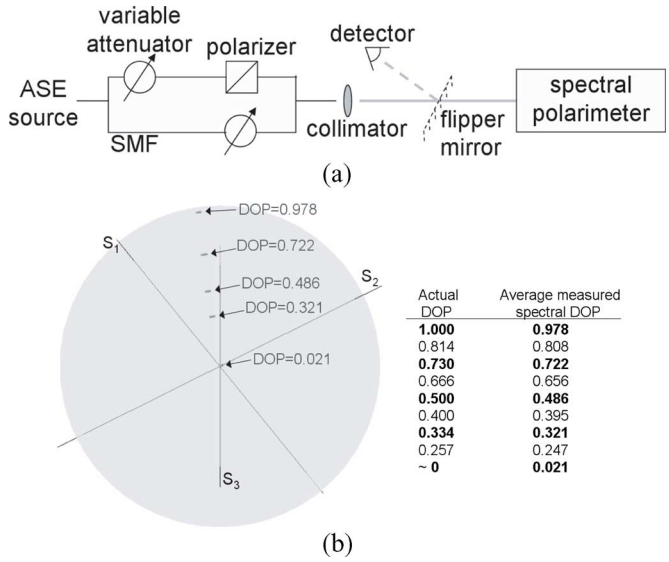

Actual DOP	Average measured spectral DOP
1.000	**0.978**
0.814	0.808
0.730	**0.722**
0.666	0.656
0.500	**0.486**
0.400	0.395
0.334	**0.321**
0.257	0.247
~ 0	**0.021**

Fig. 15. (a) Setup for producing and measuring partially depolarized light. (b) Sample measurement results of depolarized lights produced. The different clusters show different sets of spectral SOP points with DOP varying from 0 to 1.

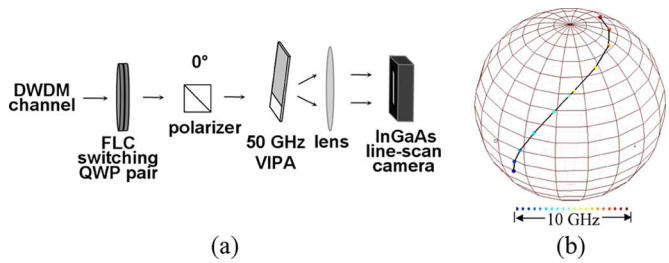

Fig. 16. (a) Schematic diagram of a high-resolution spectral polarimeter. (b) Sample spectral SOP measurement of an OC192 channel.

depolarized light. The SOP points show up inside the unit Poincarè sphere as their DOP are less than 1. Also, their SOP vectors are aligned as expected because there were no movements in the setup that could cause a SOP change during the experiment.

IV. High Spectral Resolution Configurations

So far, we have covered spectral polarimetry with resolution of tens of gigahertz. For long-haul broadband systems where spectral polarization scrambling becomes large, it may be desirable to resolve the spectral SOP profile within individual 10-Gb/s channels, which requires spectral resolution on the order of 1 GHz. For example, such resolution enables measurement of SOP strings, which have been proposed for monitoring of PMD [24]. The bandwidth and resolution scalability of our spectral polarimeter allow this device to meet various spectral specifications. For the high-resolution requirement, we substituted the diffraction grating with a 50-GHz free-spectral-range (FSR) VIPA, as shown in Fig. 16(a). We took a portable version of the high-resolution spectral polarimeter to the field and operated it in an AT&T central office [25]. The spectral SOP of four OC-192 channels were monitored each minute for three days on a 250-km fiber route carrying live traffic between two major U.S. cities. A sample of spectral SOP measurement

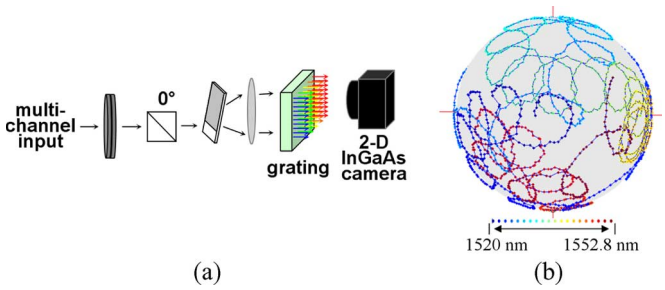

Fig. 17. (a) Schematic diagram of a broadband high-resolution spectral polarimeter. (b) Spectral SOP measurement of 1476 spectral components nearly covering the entire C-band.

of one of the channels is shown in Fig. 16(b). The string on the Poincarè sphere represents a 10-GHz bandwidth of spectral SOP taken at 1-GHz resolution. As can be shown, the spectral SOP profile is well resolved using this polarimeter. Since the principle of operation is the same for this high-resolution spectral polarimeter as the ones previously described, it requires the same calibration procedure, and the performance figures are expected to be similar. However, due to the 50-GHz FSR of the VIPA, this setup is only capable of measuring a single channel at a time. A tunable filter is needed in front of the polarimeter to monitor multiple channels, which was the method used at the AT&T central office for monitoring those four channels. Although the need for a tunable filter to select one WDM channel at a time is similar to other polarimeter designs [26], [27], our apparatus provides a high-resolution scan within each selected channel at a speed not offered by other approaches.

An alternative method, which allows the monitoring of multiple channels in parallel without a tunable filter, utilizes a VIPA in conjunction with a diffraction grating as shown in Fig. 17(a). In this setup, the VIPA periodically disperses segments of 50-GHz bandwidth in the vertical direction, and a 1100-line/mm grating is used as a coarse disperser to separate all the FSRs of the VIPA in the horizontal direction. Finally, a 2-D InGaAs camera can be used to image the 2-D spectral dispersion profile, which allows simultaneous spectral SOP monitoring of every channel over the entire C-band ($\sim$40 nm). Fig. 17(b) shows a sample of the measured results of SOP spectrally scrambled by eight concatenated sections of PM fibers with mismatched optic axes. This particular polarimeter setup yielded 1476 spectral SOP points with 2.8-GHz spacing at less than -20 dB of crosstalk between neighboring points (see [28] for a more detailed description of this design).

V. Conclusion

We have presented a spectral polarimeter design capable of performing hundreds of spectral polarization measurements within 1 ms. The SOP-only polarimeter provides spectral SOP measurements to an accuracy of within 2° over most of the wavelength within the test bandwidth of 110 nm. When wavelength-dependent DOP measurement is also of interest, the complete polarimeter design has been shown to measure spectral DOP with $< 3.5\%$ accuracy within the entire C-band at a resolution of $\sim$0.15 nm and shows little wavelength dependence at the cost of a slightly higher SOP error. This complete polarimeter design will allow both SOP and DOP monitoring of every WDM or DWDM channel within the entire C-band on a near-real-time basis. The high-resolution version of the polarimeter design has been demonstrated to track the spectral polarization variation and evolution within a single 10-Gb/s DWDM channel and can be reconfigured to perform on all channels simultaneously within the C-band at an unprecedented speed.

Acknowledgment

The authors would like to thank D. Leaird, M. Akbulut, D. Luu, P. J. Miller, H. Miao, and Y. Lin for valuable discussions and help; C. Lin from Avanex for donation of the VIPA; M. Boroditsky, M. Brodsky, and P. Magill from AT&T for allowing the authors to test the spectral polarimeter on commercial 10-GHz lightwave communication systems; and an anonymous referee for valuable comments.

References

[1] S. M. R. M. Nezam, J. E. McGeehan, and A. E. Willner, "DOP based PMD monitoring for subcarrier-multiplexed signals via equalized carrier/sideband filtering," *J. Lightw. Technol.*, vol. 22, no. 4, pp. 1078–1085, Apr. 2004.

[2] M. Akbulut, A. Weiner, and P. Miller, "Wideband all-order polarization mode dispersion compensation via pulse shaping," *Opt. Lett.*, vol. 30, no. 20, pp. 2691–2693, Oct. 2005.

[3] M. Boroditsky, M. Brodsky, N. J. Frigo, P. Magill, and L. Raddatz, "In-service measurements of polarization-mode dispersion and correlation to bit-error rate," *IEEE Photon. Technol. Lett.*, vol. 15, no. 4, pp. 572–575, Apr. 2003.

[4] N. S. Bergano, C. D. Poole, and R. E. Wagner, "Investigation of polarization dispersion in long lengths of single-mode fiber using multilongitudinal mode lasers," *J. Lightw. Technol.*, vol. LT-5, no. 11, p. 1618, Nov. 1987.

[5] L. Moller, P. Westbrook, S. Chandrasekhar, R. Dutta, and S. Wielandy, "SOP and PMD monitoring with WDM polarimeter," *Electron. Lett.*, vol. 38, no. 12, pp. 584–586, Jun. 2002.

[6] M. Boroditsky, M. Brodsky, N. J. Frigo, P. Magill, and J. Evankow, "Viewing polarization 'Strings' on working channels: High-resolution heterodyne polarimetry," presented at the European Conf. Optical Communication, Stockholm, Sweden, 2004, Session We1.4.5.

[7] C. Madsen *et al.*, "Integrated optical spectral polarimeter for signal monitoring and feedback to a PMD compensator," *J. Opt. Netw.*, vol. 3, no. 7, pp. 490–500, Jul. 2004.

[8] R. A. Azzam, A. M. El-Saba, and M. A. Abushagur, "Spectrophotopolarimeter based on multiple reflections in a coated dielectric slab," *Thin Solid Films*, no. 313–314, pp. 53–57, 1998.

[9] R. Noe, A. Maucher, and R. Ricken, "Spectral polarimeters based on integrated acousto-optical Ti:$LiNbO_3$ TE–TM converters," *Fiber Integr. Opt.*, vol. 18, no. 4, pp. 273–286, Oct. 1999.

[10] K. Oka and T. Kato, "Spectroscopic polarimetry with a channeled spectrum," *Opt. Lett.*, vol. 24, no. 21, pp. 1475–1477, Nov. 1999.

[11] I. Roudas, G. A. Piech, M. Mlejnek, Y. Mauro, D. Q. Chowdhury, and M. Vasilyev, "Coherent frequency-selective polarimeter for polarization-mode dispersion monitoring," *J. Lightw. Technol.*, vol. 22, no. 4, pp. 953–963, Apr. 2004.

[12] P. B. Phua, J. M. Fini, and H. A. Haus, "Real-time first and second order PMD characterization using averaged state-of-polarization of filtered signal and polarization scrambling," *J. Lightw. Technol.*, vol. 21, no. 4, pp. 982–989, Apr. 2003.

[13] J. Peerlings, "Polarization mode dispersion and fiber characterization," *Fiber Optic Technol.*, pp. 12–20, Dec. 2004.

[14] P. M. Crummrich, E. D. Schmidt, W. Weiershausen, and A. Mattheus, "Field trial results on statistics of fast polarization changes in long haul WDM transmission systems," presented at the Optical Fiber Communication Conf., Anaheim, CA, 2005, session OThT6.

[15] S. X. Wang and A. M. Weiner, "Fast wavelength-parallel polarimeter for broadband optical networks," *Opt. Lett.*, vol. 29, no. 9, pp. 923–925, May 2004.

[16] R. A. Chipman, "Polarimetry," in *Handbook of Optics*, 2nd ed, vol. 2. M. Bass, Ed. New York: McGraw-Hill, 1994, ch. 22, pp. 22.1–22.33.
[17] S. T. Lagerwall, *Ferroelectric and Antiferroelectric Liquid Crystals*. Weinheim, NY: Wiley, 1999.
[18] Displaytech, *Polarization Rotators*, Feb. 3, 2006. [Online]. Available: http://www.displaytech.com/downloads/PolarizationRotators.pdf
[19] X. S. Yao, L. Yan, and Y. Shi, "Highly repeatable all-solid-state polarization-state generator," *Opt. Lett.*, vol. 30, no. 11, pp. 1324–1326, Jun. 2005.
[20] S. Xiao and A. M. Weiner, "Coherent Fourier transform electrical pulse shaping," *Opt. Express*, vol. 14, no. 7, pp. 3073–3082, Apr. 2006. [Online]. Available: http://www.opticsinfobase.org/abstract.cfm?URI=oe-14-7-3073
[21] P. Watson, P. J. Bos, and J. Pirs, "Effects of surface topography on formation of zig-zag defects in SSFLC devices," in *Proc. Soc. Inf. Display Int. Symp. Dig. Tech. Papers*, 1997, pp. 743–745.
[22] G. Strang, *Linear Algebra and Its Applications*, 3rd ed. Philadelphia, PA: Saunders, 1988.
[23] P. A. Williams, *Optoelectronics Division*. Boulder, CO: NIST. (personal communication, 7/10/2002).
[24] M. Boroditsky *et al.*, "Comparison of system penalties from first and multi-order PMD," *IEEE Photon. Technol. Lett.*, vol. 17, no. 8, pp. 1650–1652, Aug. 2005.
[25] S. X. Wang, A. M. Weiner, M. Boroditsky, and M. Brodsky, "Non-intrusive estimation of pMD-induced penalty via high speed, high resolution spectral polarimeter," presented at the Optical Fiber Commun. Conf., Anaheim, CA, 2006, session SFL6.
[26] M. Petersson, H. Sunnerud, M. Karlsson, and B. E. Olsson, "Performance monitoring in optical networks using Stokes parameters," *IEEE Photon. Technol. Lett.*, vol. 16, no. 2, pp. 686–689, Feb. 2004.
[27] L. Moller *et al.*, "Method for PMD vector monitoring in picosecond pulse transmission systems," *J. Lightw. Technol.*, vol. 19, no. 8, pp. 1125–1224, Aug. 2001.
[28] S. X. Wang, S. Xiao, and A. M. Weiner, "Broadband, high spectral resolution 2-D wavelength-parallel polarimeter for dense WDM systems," *Opt. Express*, vol. 13, no. 23, pp. 9374–9380, Nov. 2005. [Online]. Available: http://www.opticsinfobase.org/abstract.cfm?URI=oe-13-23-9374

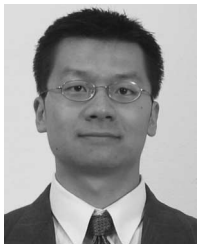

Shawn X. Wang (S'04) received the B.S. degree in electrical and computer engineering from Purdue University, West Lafayette, IN, in 2001. He is currently working toward the Ph.D. degree at the School of Electrical and Computer Engineering, Purdue University.

He has authored and coauthored 15 journal articles and conference proceedings papers. His research interests include high-speed and high-resolution spectral polarimetry, polarization mode dispersion (PMD), and PMD-related performance monitoring in lightwave communication systems.

Mr. Wang is a recipient of the Benjamin Meisner Fellowship from Purdue University (2001–2002). He serves as a frequent reviewer for the IEEE PHOTONICS TECHNOLOGY LETTERS and the JOURNAL OF LIGHTWAVE TECHNOLOGY. He is a Student Member of the IEEE Lasers and Electro-Optics Society and the Optical Society of America.

Andrew M. Weiner (S'84–M'84–SM'91–F'95) received the Sc.D. degree in electrical engineering from the Massachusetts Institute of Technology (MIT), Cambridge, in 1984.

From 1979 to 1984, he was a Fannie and John Hertz Foundation Graduate Fellow at MIT. Upon graduation, he joined Bellcore, first as member of the technical staff and later as a Manager of Ultrafast Optics and Optical Signal Processing Research. He moved to Purdue University, West Lafayette, IN, in 1992 and is currently the Scifres Distinguished Professor of Electrical and Computer Engineering. From 1997 to 2003, he served as the ECE Director of Graduate Admissions. He has published five book chapters and over 175 journal articles. He has been an author or coauthor of over 300 conference papers, including approximately 80 conference invited talks, and has presented over 70 additional invited seminars at university, industry, and government organizations. He holds eight U.S. patents. His research focuses on ultrafast optical signal processing and high-speed optical communications. He is especially well known for pioneering the field of femtosecond pulse shaping, which enables generation of nearly arbitrary ultrafast optical waveforms according to user specification.

Prof. Weiner has received numerous awards for his research, including the Hertz Foundation Doctoral Thesis Prize (1984), the Adolph Lomb Medal of the Optical Society of America (1990), the Curtis McGraw Research Award of the American Society of Engineering Education (1997), the International Commission on Optics Prize (1997), the IEEE LEOS William Streifer Scientific Achievement Award (1999), the Alexander von Humboldt Foundation Research Award for Senior U.S. Scientists (2000), and the inaugural Research Excellence Award from the College of Engineering at Purdue (2003). He is a Fellow of the Optical Society of America. He has served as Cochair of the Conference on Lasers and Electro-optics and the International Conference on Ultrafast Phenomena and as an Associate Editor of several journals. He has also served as Secretary/Treasurer of IEEE LEOS and as a Vice President of the International Commission on Optics (ICO).